Organ- and function-specific anatomical organization and bioelectronic modulation of the vagus nerve

Naveen Jayaprakash[1§], Viktor Toth[§1], Weiguo Song[§1], Avantika Vardhan[1], Todd Levy[1], Jacquelyn Tomaio[2], Khaled Qanud[1], Ibrahim Mughrabi[1], Yiela Saperstein[3], Yao-Chuan Chang[1], Moontahinaz Rob[1], Anna Daytz[3], Adam Abbas[4], Jason Ashville[5], Anna Vikatos[1], Umair Ahmed[1], Anil Vegesna[1], Zeinab Nassrallah[3], Bruce T. Volpe[1], Kevin J. Tracey[1], Yousef Al-Abed[1], Timir Datta-Chaudhuri[1], Larry Miller[1], Mary F. Barbe[6], Sunhee C. Lee[1], Theodoros P. Zanos[1], Stavros Zanos*[1]

[1] Feinstein Institutes for Medical research, Manhasset, New York. [2] The City University of New York, New York.[3] Donald and Barbara Zucker School of Medicine at Hofstra/Northwell, Hempstead, New York. [4]Jacobs School of Medicine and Biological Sciences, Buffalo, New York. [5] NYIT College of Osteopathic Medicine, Glen Head, New York. [6]Temple University, Philadelphia, Pennsylvania.

*Corresponding author. Email: szanos@northwell.edu

([§]) These authors contributed equally to this work.

Abstract

Afferent and efferent fibers in the vagus nerve travel inside fascicles and form branches to innervate organs and regulate organ functions. The spatial organization of fibers and fascicles, with respect to the functions they mediate and the organs they innervate, is unknown. Accordingly, it is unknown whether such organization can be leveraged by bioelectronic devices for function- and organ-specific neurostimulation. To characterize the functional microscopic anatomy of the vagus, we developed a pipeline consisting of micro-computed tomography imaging of fascicles and quantitative immunohistochemistry of single fibers. We found that, in swine, the vagus contains clusters of fascicles, organized along 2 overlapping functional axes: one axis specific to sensory vs. motor somatic and visceral functions, with clusters increasingly separating in the cephalad direction, and a second axis specific to innervated organs, including larynx, lungs and heart, with increasing separation in the caudad direction. Large myelinated afferents and efferents, and small unmyelinated efferents occupy large areas of specific clusters of fascicles; small unmyelinated afferents are numerous and occupy small areas across every fascicle. To test whether fiber populations can be selectively modulated, we developed a multi-contact cuff electrode accommodating the nerve fascicular structure. Stimulation targeting separate nerve sections evokes compound action potentials from fibers of distinct functional types and elicits differential organ responses, including laryngeal muscle contraction, cough reflex, and changes in breathing and heart rate. Our results indicate that vagus fibers are anatomically organized according to functions they mediate and organs they innervate and can be differentially modulated by spatially selective nerve stimulation.

Introduction

The autonomic nervous system maintains physiological homeostasis in organs and systems through an interconnected network of neural reflexes. Autonomic reflexes are comprised of sensory neurons that detect changes in physiological parameters, and motor neurons that modulate organ functions in response to physiologic changes. With its large number of afferent (sensory) and efferent (motor) fibers, the vagus is the main conduit for bidirectional communication between the brain and body organs and participates in autonomic reflexes regulating cardiorespiratory, gastrointestinal and neuroimmune functions. In the human vagus, nerve fibers are arranged in fascicles, longitudinal bundles within the nerve separated by connective tissue [1, 2]. Along the cervical and thoracic vagus, afferent and efferent fibers leave the fascicles and emerge from the nerve trunk to form branches, which in turn provide sensory and motor innervation to the heart, the airways and the lungs [3, 4]. Even though much is known about the macroscopic and microscopic anatomy of the vagus, the spatial organization of fascicles and fibers within the nerve, as it relates to the innervated organs and the sensory and motor functions of the vagus, is largely unknown.

The spatial organization of fibers in the human vagus has implications for therapies based on nerve stimulation. Bioelectronic therapies consist of implanted electrode devices that deliver electrical energy to the vagus to alter activity of nerve fibers and modulate organ function in diseases in which the vagus is implicated, like heart failure [5], inflammatory bowel disease [6] and rheumatoid arthritis [7]. However, current vagus stimulation devices deliver electrical energy all around the nerve, without regard for how nerve fibers are organized, often resulting in clinically significant side effects from non-targeted organs [8-12]. For instance, a vagus stimulation device tested in patients with heart failure produced side effects from the airways by activating laryngeal nerve fibers; that prevented investigators from delivering higher stimulus intensities required to activate cardioprotective nerve fibers, thereby limiting therapeutic efficacy [13]. Electrode devices that accommodate the anatomical organization of the vagus could target specific sub-populations of nerve fibers and lead to reduced side-effects [9, 14], expand the indications of nerve stimulation to organs not targeted by existing therapies [15, 16], and allow the mechanistic study of specific parts of autonomic reflexes in health and disease.

In this study, we developed a large scale, quantitative pipeline to characterize the anatomical organization of the vagus at the level of organ branches, fascicles and fiber types and applied it on the vagus of the swine, the preferred animal model for the human vagus [2, 10]. We discovered rich organization of fibers within the vagus, with fascicles and fibers clustered in separate groups, with respect to the specific physiological functions they mediate and the organs they innervate. We then developed a multi-contact cuff electrode device that accommodates the spatial organization of fascicles in the vagus and used it to deliver spatially selective nerve stimulation. By targeting different sections of the nerve, we were able to evoke compound action potentials from nerve fibers of different functional types and elicit differential responses from organs innervated by the vagus.

Results

Fascicles form organ-specific clusters along the vagus

The vagus in swine is highly fascicular, with 40-50 fascicles of varying sizes in the cervical region [Suppl. Figure S1]. Branches derived from the cervical and thoracic vagus provide sensory and motor innervation to visceral organs [4], including the larynx and pharynx, through the superior and recurrent laryngeal nerves [17], the heart, through the cardiac branch [4, 18], and the lower airways and lungs, through the bronchopulmonary branches [19]. To understand the spatial arrangement of fascicles with respect to the formation of vagus branches, we performed high resolution micro-computed tomography (micro-CT) imaging of the vagus nerve trunk, from above the nodose ganglion, rostrally, to the lower thoracic portion of the nerve, caudally. Fascicles with any visible contribution to the formation of vagus branches were manually annotated at individual sections taken through the branching point (Suppl. Figures S2, S3, S4) and were considered to project to the corresponding organ (Figure 1A). The longitudinal trajectories of those fascicles were then tracked along the length of the vagus rostrally with the use of an automated image segmentation algorithm.

The longitudinal trajectories of many of the fascicles in the vagus trunk are not straight but helical (Suppl. Video 1). Fascicles contributing to the bronchopulmonary (BP) branch form a cluster close to its level of entry (yellow fascicles, Figure 1B, panels x and w; and Figure 1C, panels r and q); bronchopulmonary fascicles remain clustered for several centimeters rostrally (Figure 3B, panels v-s; Figure 3C, panels p-o). The recurrent laryngeal nerve (RNL) joins the trunk by contributing another cluster of fascicles (red fascicles; Figure 1B, panels r-q; Figure 1C, panels n-m). Some of those fascicles ascend in parallel to the BP cluster and some merge with it, in a “mixed” BP-RLN cluster (orange fascicles; Figure 1B, panels p-o; Figure 1C, panels m-l). Both BP and RLN fascicles disappear within a few centimeters and are replaced by a cluster of combined BP-RLN fascicles which runs rostrally along the upper thoracic (Figure 1B, panel n) and the cervical vagus (Figure 1C, panel l). The cardiac branch joins the vagus trunk rostrally to the RLN entry and forms a separate cluster of fascicles (blue fascicles; Figure 1B, panel o; Figure 1C, panel l). Some of the cardiac fascicles maintain their separate trajectories all the way through the upper thoracic and cervical vagus (Figure 1B, panels l-d; Figure 1C; panels k-d) and some merge with the mixed BP-RLN fascicles to form a larger cluster of mixed BP-RLN-cardiac (green fascicles; Figure 1B, panels m and above; Figure 1C, panels e and above). Many of the mixed BP-RLN-cardiac fascicles terminate in the nodose ganglion, and some of them bypass it (Figure 1B, panels b, a; Figure 1C, panels b, a). Fascicular branching, where one fascicle branches to form two fascicles, or fascicular merging, where two fascicles merged to form one fascicle is observed throughout the length of the nerve (Suppl. Figure S5, and Supplementary video 1). These findings indicate that fascicles in the thoracic and cervical vagus trunk form spatially distinct organ-specific clusters close to the levels of entry of branches to those organs; clusters progressively merge into larger mixed clusters in the rostral direction.

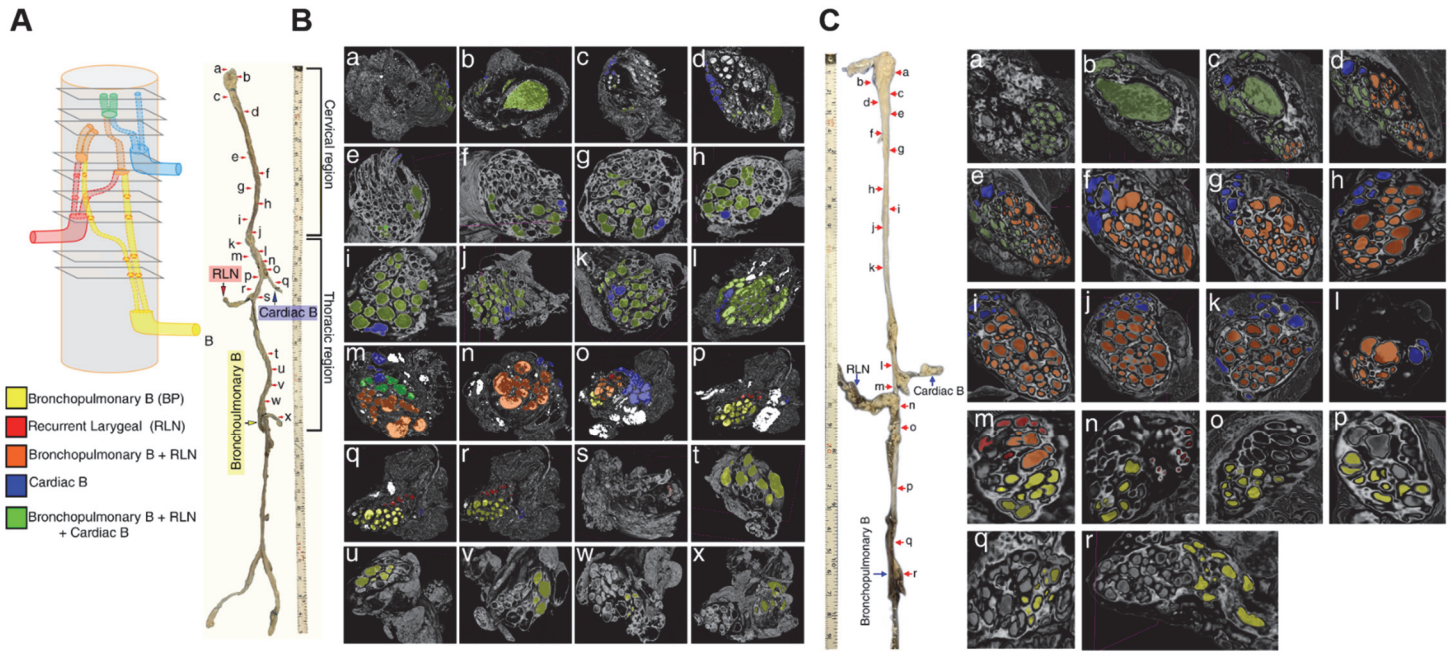

Figure 1. Fascicles form organ-specific clusters along the vagus. (A) Schematic showing a segment of the vagus trunk with 3 branches joining it (bottom to top): bronchopulmonary (BP, yellow), recurrent laryngeal nerve (RLN, red), cardiac branch (blue). The trajectories of fascicles contributing to each branch were traced rostrally inside the trunk, even after they merged with other fascicles to form "mixed" fascicles: BP and RLN (orange), BP, RLN and cardiac (green). (B) Macroscopic structure of an intact right vagus trunk, from the nodose ganglion to the lower thoracic level (left). On the right, multiple micro-computed tomography sections through the trunk are shown (panels a-x), with fascicles contributing to each of the identified branches or combinations of branches shaded in the corresponding colors. (C) Macroscopic and fascicular structure of an intact left vagus trunk from a second animal.

Fascicles form separate afferent and efferent clusters along the vagus

To understand the spatial arrangement of fascicles with respect to sensory or motor functions, we analyzed the micro-CT images in the opposite direction, from rostral to caudal: fascicles that originate in the nodose ganglion were considered primarily afferent and those that bypass the nodose ganglion were considered primarily efferent (Figure 2A; Figure 2B, a, b). By tracking the trajectories of fascicles in the caudal direction, we found that afferent and efferent fascicles form 2 separate clusters throughout most of the cervical vagus (Figure 2B, c-i); the 2 clusters begin to merge in the lower cervical region (Figure 2B, j, k), and the afferent-efferent separation gradually disappears in the thoracic region (Figure 2A, l-o). Similar results from a second nerve are shown in Suppl. Figure S23.

To examine whether the separation of afferent and efferent fascicles persists at the single fiber level, we performed immunohistochemistry (IHC) in sections through the nodose ganglion, mid-cervical and thoracic region (Figure 2B, Suppl. Figure S6 and S7). At the nodose ganglion level (Figure 2B, a), ChAT-positive (ChAT+) fibers, indicative of efferent function, are almost absent (Figure 2B, b1), however Nav1.8-positive (Nav1.8+) sensory "pseudo-unipolar" cells are numerous (Figure 2B, b2; Suppl. Figure S8). In an efferent fascicle, ChAT+ fibers are abundant (Figure 2B, c1); Nav1.8+ fibers are seen but are not as common (Figure 2B, c2). At the mid-cervical region (Figure 2B, d), fascicles poor in ChAT+ fibers (Figure 2B, e1) but rich in Nav1.8+ fibers (Figure 2B, e2) are separated from fascicles rich in ChAT+ (Figure 2B, f1) and in Nav1.8+ fibers (Figure 2B, f2). Finally, at the thoracic region, all fascicles show intense staining for both ChAT and Nav1.8 (Figure 2B, g-i; Suppl. Figure S10). These findings indicate that afferent and efferent fascicles form spatially distinct clusters in the upper and mid-cervical trunk of the vagus; the clusters become progressively less

separated in the lower cervical region, and in the thoracic region the afferent-efferent separation of fascicles disappears.

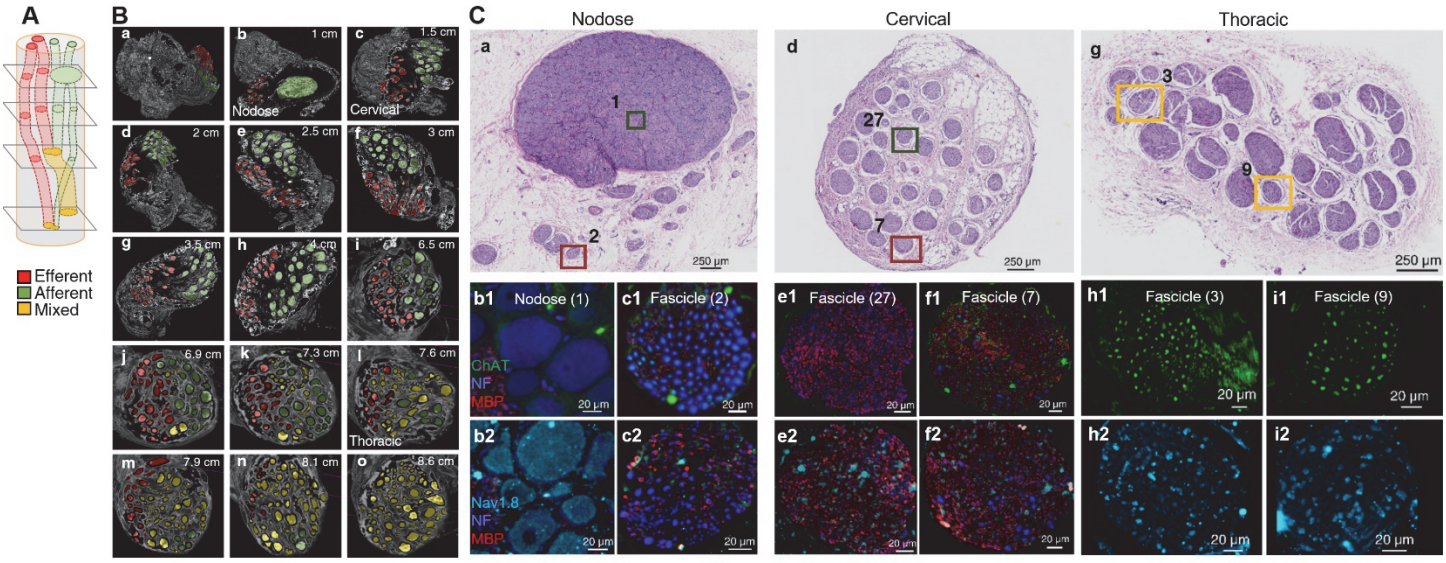

Figure 2. Afferent and efferent fascicles form clusters along the vagus. (A) Schematic showing a segment of the vagus trunk with several fascicles along its path; afferent fascicles (green) converge into the nodose ganglion, while efferent fascicles (red) by-pass the nodose. At more caudal levels, afferent and efferent fascicles merge to form mixed fascicles (yellow). (B) Micro-computed tomography imaging of an intact right vagus trunk, from just above the nodose ganglion to the upper thoracic level. Panels (a-i) show the trajectories of afferent and efferent fascicles in consecutive sections through the cervical vagus, at different levels (shown in cm from the rostral end of the sample). (C) Imaging of afferent and efferent fiber populations in afferent and efferent fascicles. (a) H&E section at the level of the nodose ganglion. An area inside the ganglion (1) and an efferent fascicle (2) are selected. (b1) Nodose area stained with an "efferent" panel of antibodies for immunohistochemistry (IHC), consisting of anti-neurofilament antibody (NF, blue) that labels nerve fibers, anti-myelin basic protein antibody (MBP, red) that labels myelin, and choline-acetyl-transferase (ChAT, green) that labels efferent, cholinergic, fibers. (b2) The same nodose area stained with an "afferent" IHC panel, consisting of NF, MBP and anti-Nav1.8 antibody (cyan) that labels afferent fibers and sensory neurons. (c1) Fascicle (2) stained with an efferent IHC panel. (c2) Fascicle (2) stained with an afferent IHC panel. (d) H&E section at the mid-cervical level. An afferent (27) and an efferent fascicle (7) are selected. The 2 fascicles are stained with an efferent (e1 and f1, respectively) and an afferent IHC panel (e2 and f2, respectively). (g) H&E section at the thoracic level. Two fascicles are selected, stained with an afferent (h1, i1) and an efferent (h2, i2) IHC panel.

Nerve fibers of different functional types are specifically organized across and within fascicles in the cervical vagus

The human and swine vagus contain fibers of several functional types, including myelinated and unmyelinated afferents and efferents [1, 9, 11]. Myelinated efferents provide motor innervation to laryngeal muscles (Aα-type) or parasympathetic innervation to visceral organs (B-type); unmyelinated efferents are primarily sympathetic fibers to visceral organs (C-type). Myelinated afferents convey somatic sensation from the pharyngeal and laryngeal mucosa (Aβ-type) or visceral sensation from mechanical and chemical receptors in organs (Aδ-type); unmyelinated afferents convey nociception and temperature and chemical sensation from visceral organs (C-afferents). To understand the spatial organization of vagus fibers of different types in the cervical region, the most common anatomical location for stimulation electrodes, we developed a quantitative IHC pipeline, consisting of IHC staining, imaging and automated fiber segmentation, feature extraction and analysis, at the single fiber level. Based on the expression pattern of fiber-specific IHC markers, we classified each fiber in the vagus as myelinated efferent (MEff, Figure 3A,a), myelinated afferent (MAff, Figure 3A, b),

unmyelinated efferent (UEff, Figure 3A, c) or unmyelinated afferent (UAff, Figure 3A, d and 3B; Suppl. figure S11). Applying additional fiber diameter criteria, we classified fibers in even more specific functional types, compatible with the Erlanger-Gasser scheme (Table I).

	A	B	C	D	E	F	G	H	I				
	Fiber type	Erlanger Gasser class.	Side	% Fiber area in nerve, mean [range]	Fiber count in nerve, mean [range]	% Fiber count in nerve, mean [range]	% Fiber area in fascicle, mean [range]	Fiber count in fascicle, mean [range]	Fiber type features				
									NF	MBP	ChAT	Nav1.8	Diameter (μm), mean (IQR)
1	Myel. eff. (MEff)	Aα, Aγ & B	L R	33 [28–35] 31 [15–43]	14.8K [12.7–16.6] 14.6K [4.9–21.4]	4.2 [2.7–6.4] 5.1 [0.7–8.7]	29 [0–83] 29 [0–83]	335 [0–2,419] 403 [0–1,879]	+	+	+	NA	3.47 (1.46)
2	>10 μm	Aα	L R	1.9 [0.4–4.6] 1.8 [0.5–4.5]	52 [12–130] 54 [12–127]	0.01 [0–0.03] 0.01 [0–0.02]	1.25 [0–27] 1.20 [0–19]	1.2 [0–33] 1.5 [0–21]	+	+	+	NA	15.7 (5.93)
3	<3 μm	B	L R	15 [12–20] 16 [4–27]	11.6K [9.5–13.5] 11.8K [3.4–18.7]	3.3 [2.0–5.2] 4.2 [0.5–7.6]	13.8 [0–48] 14.5 [0–57]	14 [0–48] 32 [0–57]	+	+	+	NA	3.06 (1.05)
4	Myel. aff. (MAff)	Aβ & Aδ	L R	52 [50–56] 58 [48–74]	34.0K [29.7–37.6] 28.7K [25.8–31.4]	9.1 [7.8–11.2] 8.7 [5.2–10.5]	54 [0–86] 59 [12–92]	766 [0–2,753] 790 [20–3,401]	+	+	–	NA	3.10 (1.42)
5	>5 μm	Aβ	L R	3.6 [1.2–5.7] 14 [1.7–36]	409 [163–623] 1,348 [178–3,109]	0.10 [0.06–0.14] 0.30 [0.02–0.59]	3.1 [0–20] 10 [0–54]	9 [0–56] 37 [0–510]	+	+	–	NA	8.49 (2.98)
6	2-5 μm	Aδ	L R	40 [37–42] 37 [33–42]	20.4K [17.7–22.4] 17.6K [13.9–21.2]	5.5 [4.7–6.8] 5.3 [3.2–7.1]	41 [0–72] 40 [0–83]	41 [0–72] 48 [0–84]	+	+	–	NA	3.72 (1.21)
7	Unmyel. eff. (UEff)	C-Symp.	L R	6.9 [5.1–8.8] 4.7 [2.9–7.4]	21.8K [15.1–25.7] 15.8K [10.8–23,3]	6.3 [3.1–9.8] 4.9 [2.4–7.8]	8.9 [0.6–54] 6.6 [0.7–35]	492 [9–3,084] 434 [26–1,626]	+	–	–	NA	1.83 (0.78)
8	Unmyel. aff. (UAff)	C-Aff.	L R	7.6 [5.1–10.2] 6.3 [5.1–7.9]	315K [190.0–414.0] 294K [186.0–470.0]	80 [72–86] 81 [75–91]	7.2 [1–28] 5.3 [1–16]	7.0K [2.0–63.0] 8.0K [2.0–78.0]	–	–	NA	+	0.55 (0.32)

Table I. Fiber counts and associated areas of coverage, relative and absolute, of different fiber types in the cervical vagus. Different fiber types (rows 1-8) according to criteria used in our pipeline (A) and corresponding fiber types according to Erlanger-Gasser classification (B). (C) Nerve side (left or right). (D) Percentage of fiber-covered area in the entire nerve corresponding to a given fiber type; shown is mean and range across 8 nerves. (E) Absolute fiber count of given fiber type in the entire nerve. (F) Percentage of given fiber type among all fibers in the whole nerve. (G) Percentage of area covered by given fiber type in single fascicles; mean [range] across all fascicles, of all nerves. (H) Absolute count of given fiber type in single fascicles. (I) Fiber type-specific features used in our pipeline to classify single fibers: positive (+) or negative (-) in NF stain, MBP (myelin basic protein) stain, ChAT (choline-acetyl-transferase) stain, and Nav1.8 stain. Measured diameters for each fiber type (in μm, mean and interquartile range).

Overall, we counted 200-450K individual fibers in each nerve, with roughly 70-85% of them of the UAff type; however, UAff fibers occupy less than 10% of the total fiber-covered area in the nerve (table I). On the other hand, myelinated fibers, MAff and MEff, despite representing less than 15% of total fiber count, occupy 60-80% of fiber-covered area (table I; and Suppl. Figure S12). There is substantial variability in fiber counts and in occupied areas across fascicles, for all fiber types. In both left and right cervical vagus, fascicles with large MEff fiber counts are clustered together on one side of the nerve (Figure 3C, a1 and a2), in agreement with our micro-CT and qualitative IHC findings (Figure 2). The few, larger Aα-type efferents are concentrated in a few fascicles within the cluster (Figure 3C, bottom left in a1 and a2), whereas the smaller, B-type fibers are more uniformly distributed within the fascicles of the efferent cluster (Figure 3C, bottom right in a1 and a2). Fascicles with large MAff fiber counts are clustered in the opposite side of the nerve (Figure 3C, b1 and b2). MAff fibers include intermediate size Aδ-type fibers, uniformly distributed within the afferent cluster (Figure 3C, bottom left in b1, b2), and the fewer, larger Aβ-type fibers, concentrated in a subset of fascicles in that cluster (Figure 3C, bottom right in b1, b2). UAff fibers are present in practically all fascicles, even though their fiber counts vary between 55% and >80% (Figure 3C, d1 and d2). Fiber distribution fascicular maps from other nerves are given in Suppl. Figure S13. More than 50% of all fibers in the nerve, independently of fiber type, lie within 500 μm from the epineurium (Suppl. Fig. S14 & S15). The fascicular distribution of UEff fibers follows that of MAff and opposes that of MEff fibers (Figure 3C, c1 and c2): counts of UEff fibers in individual fascicles are negatively

correlated with those of MAff fibers (Figure 3D, a) and positively correlated with those of MEff fibers (Figure 3D, b). The localization of UEff fibers together with MAff fibers and away from MEff fibers is observed even at the sub-fascicular level: sectors within a fascicle with high UEff counts tend to have low MEff counts (Figure 3E, a) and high MAff counts (Figure 3E, b). Within sub-fascicular sectors, fibers of the same type tend to cluster together (main diagonal of Figure 3E, c; Suppl. Figure S16). Taken together, these findings indicate that there are consistent, specific patterns in the way fibers are organized in the cervical vagus. Myelinated fibers mediating somatic and visceral sensory and motor functions are organized in separate clusters of fascicles. Sympathetic fibers co-localize with MAff and away from MEff fibers, both in entire fascicles and in sub-fascicular sectors. UAff fibers are distributed across all fascicles.

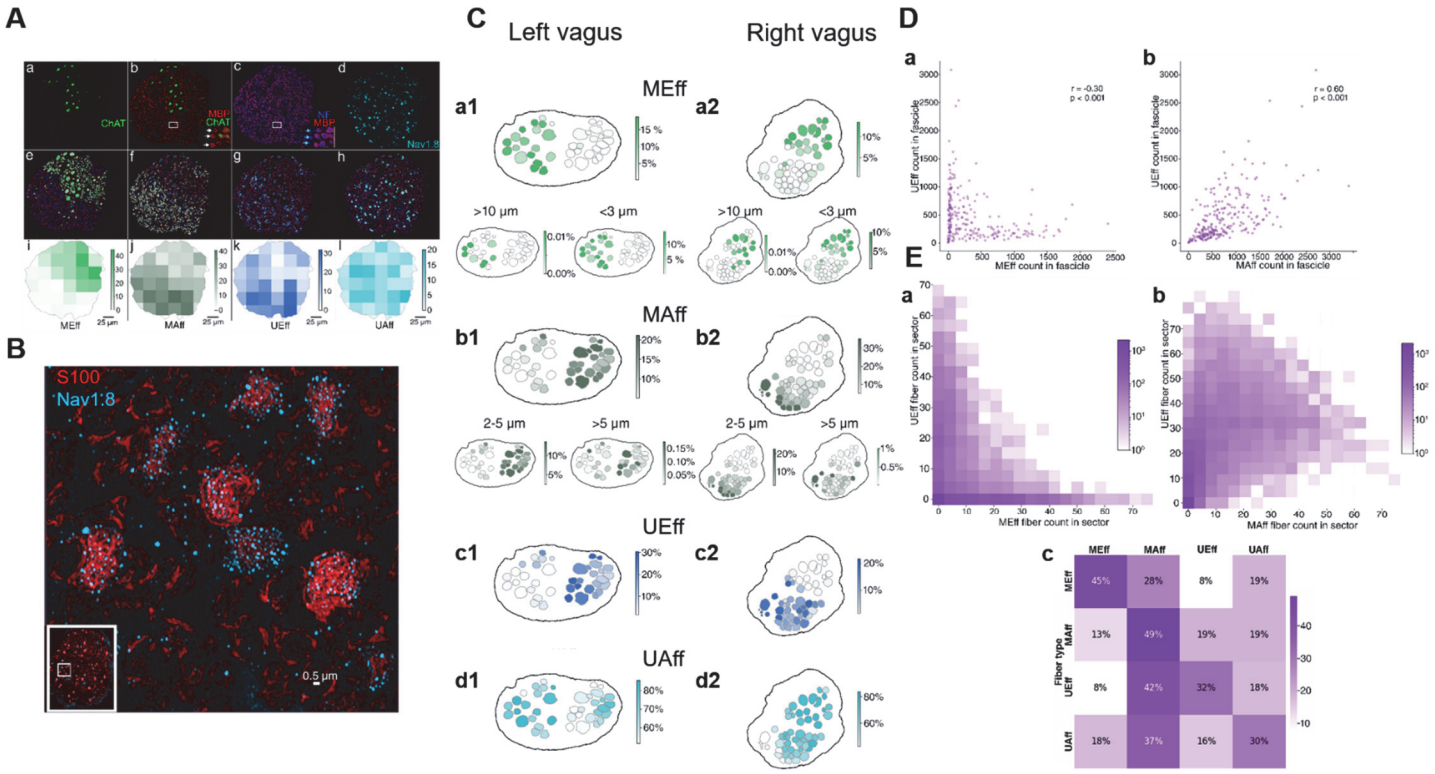

Figure 3. Functional nerve fiber types are specifically organized in the cervical vagus nerve. (A) A large-scale immunohistochemistry (IHC) and analytical pipeline was used to image, identify, characterize and classify all fibers in every fascicle. (a) ChAT+ fibers (Suppl. Figure S17) that were also NF+ and MBP+ (NF and BMP channels are not shown for clarity) were classified as myelinated efferents (MEff). (b) NF+ and MBP+ fibers that were ChAT- were classified as myelinated afferents (MAff); arrows point to single MAff fibers in inset. (c) NF+ and MBP- fibers were classified as unmyelinated efferents (UEff); arrows point to single MEff fibers in inset. (d) Nav1.8+ and MBP- fibers were classified as unmyelinated afferents (UAff). Unmyelinated afferent fibers did not stain for NF (Suppl. Fig. S18). (panels e-h) Individual fibers of each type were identified, and their features (e.g. size) and location in the fascicle were extracted. This allowed us to assess for different fiber types statistics of fiber counts, the area they cover and distributions across fascicles. (panels i-l) Local density values of each fiber type were extracted from fiber counts and locations, and projected on a fascicle using a color scale. This allowed us to assess within-fascicle arrangement of different fiber types. (B) IHC imaging of UAff fibers in a section of a nerve fascicle. Stains for Nav1.8, specific to afferent fibers, and S100, a marker of Schwann cells, are shown superimposed to reveal several Remak bundles, within which individual UAff fibers are surrounded by the cytoplasm of Schwann cells. Inset shows the entire nerve fascicle. (C) Counts of fibers of different types in the fascicles in a section from the left and the right cervical vagus trunk of the same animal. (a1) Counts of MEff fibers across fascicles of the left vagus, as percentage of total number of fibers in each fascicle; percent counts represented by a color intensity scale. Top: Counts of all MEff fibers, independently of diameter. Bottom left: Counts of MEff fibers with diameter>10μm (Aα-type). Bottom right: Counts of MAff fibers with diameter<3μm (B-type). (a2) Same as a1, but for the right vagus. (b1)

Counts of MAff fibers across fascicles of the left vagus. Top: for all MAff fibers; bottom left: for MAff fibers with diameters 2-5μm (Aβ-type); bottom right: for MAff fibers with diameters >5μm (Aδ-type). (b2) Same as b1, but for the right vagus. (c1) Counts of UEff fibers across fascicles of the left vagus, and (c2) of the right vagus. (d1) Counts of UAff fibers across fascicles of the left vagus, and (d2) of the right vagus. (D) Distinct relationships in co-localization of different fiber types across fascicles. (a) Anti-correlated counts of MEff fibers in a fascicle (abscissa) vs. counts of UEff fibers in the same fascicle (ordinate). Each point represents a single fascicle. Shown are data from all fascicles in the cervical vagus of 4 animals (8 nerves). (b) Correlated counts of MAff and UEff fibers. (E) Distinct relationships of co-localization of different fiber types within fascicles. (a) Counts of MEff and UEff fibers within a 30-μm-square fascicular sector in all analyzed fascicles. The color intensity of each pixel represents the frequency of the specific combination of MEff-UEff fiber counts: the lighter the color, the less frequent that combination is across sectors. Shown are data from all sectors within all fascicles, from all nerves. (b) Correlated counts of MAff and UEff fibers within a 30-μm-square sector. (c) Joint probability of co-localization of different fiber types within a 30-μm-square sector. In each row, color intensity and percentage values represent the probability of finding a fiber of each of the 4 types in the immediate vicinity of the fiber type represented by that row.

Spatially selective vagus nerve stimulation differentially activates organ- and function-specific fibers

Activation by bioelectronic devices of different populations of efferent and afferent fibers innervating visceral organs determines the effects of vagus neuromodulation therapies. Having demonstrated that vagus fibers have an organ- and function-specific anatomical organization, we next sought to test whether spatially selective VNS can differentially activate fibers innervating specific organs, as well as fibers for controlling sensor or motor functions. Intraneural electrodes are not well characterized with respect to their elicited stimulation effects [20] and may be associated with an increased risk of nerve injury [21]; given that >50% of fibers lie within 500 μm from the epineurium (Suppl. Figure S14 & S15), we developed an epineural nerve cuff electrode to deliver spatially selective nerve stimulation. The helical cuff included 8 contacts evenly distributed around the circumference and 2 ring-shaped return contacts (Figure 4A). The 8-contact electrode configuration was chosen because, in conceptual models of the 2-D overlap between fascicles and electrical fields generated by epineural contacts (Suppl. Figure S19A), it attained significantly higher overall efficacy compared to designs with fewer contacts (Suppl. Figure S19B, a), with the same selectivity as designs with more contacts (Suppl. Figure S19B, b); finally, it is compatible with the fascicular anatomy of the human cervical vagus (Suppl. Figure S19B, c).

Stimulation through different contacts in the multi-contact electrode produces different physiological responses specific to organs receiving vagus innervation: changes in heart rate and in blood pressure (heart and vessels), changes in breathing rate (lungs), and contraction of laryngeal muscles (Figure 4B). Stimulation elicits evoked compound action potentials (eCAPs), recorded through a second cuff electrode placed at a distance from the stimulating device, reflecting direct activation of different fibers. Depending on which contact is used for stimulation, differential activation of fast fibers, with a conduction velocity compatible with that of Aα/β-type fibers, and of slow fibers, compatible with Aδ/B-type fibers, is observed (Figure 4C). Graded physiological organ responses and, accordingly, amplitudes of fibers mediating those responses are observed at a range of stimulus intensities, resulting in recruitment curves that are different between contacts (Figure 4D; Suppl. Figure S20). Threshold intensities for eliciting organ responses [22] were determined for each contact and were plotted on a polar map representing the “directionality” of responses around the nerve (Figure 4E). Organ-specific physiological responses have different thresholds, and those thresholds depend on which contact is used for stimulation, resulting in asymmetric maps; also, maps have different shapes, depending on which organ’s response is considered (Figure 4E). In each animal, the radial location of the contact associated with the lowest heart rate threshold (heart-specific location) was arbitrarily placed at 12 o’clock (90° angle) in the polar plot. After aligning polar plots in each animal by that contact and normalizing responses between a

minimum and maximum value, we then compiled average maps of the directionality of organ responses across animals (Figure 4F). The vector sum of average heart rate thresholds points towards the location with the greatest threshold and away from the “heart-specific” location, which lies at an angle of 134° (Figure 4F, a). The lung-specific location lies at an angle of 155° (Figure 4F, b) and the larynx-specific location lies at an angle of 65° (Figure 4F, c). The directionality map for the blood pressure response is similar to that for heart rate (Figure 4F, d). Stimulus-elicited CAPs also depend on the stimulated contact, which reflects in differential recruitment of fast and slow fibers (Figure 4G). After aligning data in individual animals by the contact with the maximum fast fiber amplitude (placed at 90° angle) and normalizing fiber amplitudes, we compiled maps of the directionality of fast and slow fiber responses in several animals. The fast fiber-specific location lies at 90° (Figure 4G, a), and the slow fiber-specific location at 154° (Figure 4G, b). To test whether selectivity of nerve stimulation remains consistent across multiple days, we performed chronic vagus implants with the multi-contact cuff electrode device in 2 animals. By stimulating through different contacts during awake experimental sessions, we found that threshold intensities for eliciting the cough reflex, whose sensory arc is mediated by vagal MAff fibers innervating the laryngeal and pharyngeal mucosa, are asymmetrically distributed around the nerve and, despite the gradual increase in thresholds, the overall shape of the spatial distribution is maintained for up to 3 weeks post-implantation (Suppl. Figure S20). These findings indicate that the highly nonuniform spatial organization of fascicles and fibers in the vagus can be leveraged with a multi-contact cuff electrode to elicit differential nerve responses from vagus-innervated organs and functional fiber types.

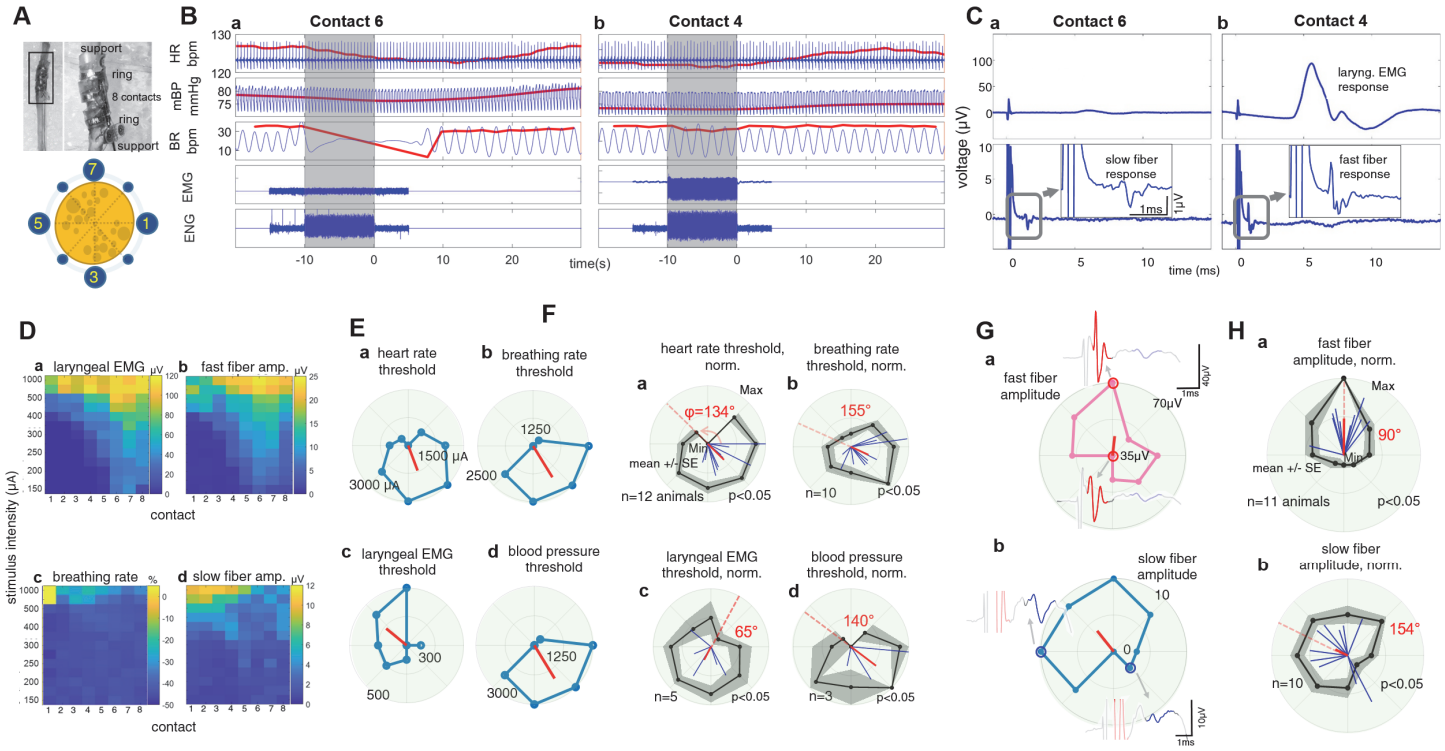

Figure 4. Spatially selective vagus nerve stimulation differentially activates organ- and function-specific fibers.

(A) Helical multi-contact cuff electrode device placed on the cervical vagus (left); the device is comprised of 2 outer support loops, 2 ring-shaped contacts, and 8 small square contacts, circumferentially placed around the nerve (right). (B) (a) Cardiovascular, respiratory and laryngeal physiological responses to a stimulus train (shaded area) through one of the 8 contacts (contact 6) include drop in heart rate (HR), a moderate drop in mean blood pressure (BP) and slowing of breathing rate (BR); at the same time, minimal evoked laryngeal muscle activity (EMG) and strong evoked responses in the nerve potential (ENG) were observed. (b) Responses to the same stimulus train delivered through a different contact

(contact 4) included minimal drop in HR, BP and BR but strong laryngeal EMG. (C) (a) Evoked laryngeal EMG (top) and compound nerve action potential (eCAP, bottom) triggered by stimuli in the train delivered to contact 6. No EMG is generated and the eCAP shows a response at a latency consistent with slow A-fiber activation. (b) EMG and eCAP triggered by stimuli delivered to contact 4; EMG response and a short latency eCAP, consistent with fast A-fiber activation, are observed. (D) Physiological responses and eCAPs mediating them have different recruitment curves from different contacts. (a) Amplitude of laryngeal EMG is shown for different stimulation contacts (abscissa) and at different intensities (ordinate), represented by the color scale. (b) Same for amplitude of fast fiber response in the eCAP; fast fibers (e.g. Aα) mediate efferent signaling to laryngeal muscles. (c) Same for the magnitude of breathing response, quantified as % change in BR. (d) Same for amplitude of slow fiber response in the eCAP; slow fibers (e.g., Aδ) mediate afferent signaling to the brain that, through a reflex mechanism (Herring-Breuer reflex) slows down or arrests breathing. (E) Example in a single animal of threshold intensities for different physiological responses, as determined for each of the 8 contacts in the multi-contact cuff electrode. (a) threshold for HR response, (b) BR threshold, (c) laryngeal EMG threshold, (d) BP threshold. Threshold was defined as the minimum intensity of a stimulus train (200 μs pulse width, 30 Hz) that produces a change of 5-10% in the corresponding physiological variable. The contact with minimum HR threshold is placed at 12 o'clock direction (origin of polar plot); the remaining plots are aligned to that orientation. In each polar plot, the origin represents the minimum threshold (e.g. 1500 μA for HR threshold, 1250 μA for BR threshold), and the outer circle the maximum threshold (e.g. 3000 μA for HR threshold, 2500 μA for BR threshold). Each point in the polar plots is the average determined from 3-5 stimulus trains delivered to each contact. The red line represents the resultant (vector sum) of thresholds across all eight contacts: its direction points towards the side of the nerve with the highest thresholds overall, i.e. away from the side that is most selective for that physiological response. (F) (a) Average (+/-SEM) normalized HR thresholds and resultant vectors in 12 individual animals. Each blue vector represents the resultant of HR thresholds around the nerve in a single animal. The red vector represents the sum of all individual resultant vectors, and it points towards the side of the nerve with the largest heart rate threshold; the dashed line opposite to that, and the associated angle, represents the most cardiac selective direction. p-value represents statistical significance of 1-way ANOVA (dependent variable: threshold, independent variable: contact angle). (b) Average BR thresholds and resultant vectors from 10 animals. (c) Average laryngeal EMG thresholds and resultant vectors from 5 animals. (d) Average blood pressure thresholds and resultant vectors from 3 animals. (G) Example in a single animal of eCAP responses and fiber amplitudes, elicited from different contacts. (a) Traces of eCAPs elicited by stimulation delivered to 2 different contacts located at the 12 and 6 o'clock directions, with the fast (red) fiber components highlighted. Polar plot of the amplitudes of fast fiber responses, ranging between minimum (origin) and maximum (outer circle). The contact eliciting the maximum fast fiber response is placed at 12 o'clock direction. The red vector represents the resultant vector of fast fiber amplitudes from all 8 contacts. (b) Same as (a), but for amplitudes of slow fiber responses. The 2 polar plots are aligned by the 12 o'clock contact. (H) (a) Average (+/-SEM) normalized eCAP response amplitudes for fast fibers (shaded trace) and resultant vectors (blue vectors) from 12 individual animals. Before averaging, individual polar plots were aligned to the contact associated with the maximum fast fiber response. The red vector represents the sum of all individual resultant vectors. p value represents statistical significance of 1-way ANOVA (dependent variable: fiber response amplitude, independent variable: contact angle). (b) Same as (a), but for slow fibers. Plot is aligned by the contact associated with the maximum fast fiber response (12 o'clock in panel (a)).

Discussion

In this study we demonstrate rich structure in the organization of fascicles and fibers in the swine vagus, with implications for the functional anatomy of autonomic reflexes. We also show that vagus nerve stimulation using a multi-contact cuff electrode device in swine leverages the structure of the vagus to differentially engage fibers of distinct functional types projecting to different organs, with potential implications for vagus neuromodulation therapies. We chose the swine model because the swine vagus more closely resembles the human in its fascicular structure, effective diameter and relative thickness of the endoneurium, perineurium and epineurium, compared to rodents and non-human primates [2, 10]. On the other hand, the swine vagus has 5-10 times more fascicles than the human vagus and accordingly smaller fascicle diameters (Suppl. Figure 1), thereby representing an appropriate anatomical substrate for testing methods and technologies for selective vagus neuromodulation [1, 9, 15, 23, 24].

A first level of organization of the vagus concerns the branches that emerge along its course: cervical branches, including the superior and recurrent laryngeal nerves for the larynx and pharynx [10, 25], thoracic branches, including the cardiac and bronchopulmonary nerves for the heart and the respiratory system, and numerous lower thoracic and abdominal branches, innervating organs of the gastrointestinal system [1]. By imaging fascicles contributing to individual branches with micro-CT [3] and then tracking trajectories of individual fascicles along the nerve trunk, we discovered that organ-specific fascicles form clusters close to the level at which those branches emerge and progressively merge with clusters from other organs, at more rostral levels (Figure 1). Cardiac fascicles are an exception, as some of them do not merge with other fascicles (Figure 1), an attribute that may facilitate selective vagus nerve stimulation for cardiac diseases [26]. Recently, it was found that fascicles contributing to the formation of laryngeal nerves in swine are grouped separately from other vagus fascicles [10]. Our findings suggest that such separation may be a manifestation of the organ-specific clustering of fascicles. The presence of a “viscerotopic” organization of fibers in the trunk of the vagus is reminiscent of the topographic organization of motor vagal neurons in the dorsal motor nucleus of the brainstem [27, 28] and of sensory vagal neurons in the nodose ganglion [28] and the nucleus tractus solitarius [29]. The progressive merging of fascicles from different organs suggests that, with regard to organ innervation, the cervical vagus is organized, at a large scale, in a “lattice-like” manner (Figure 1A).

A second level of organization of the vagus concerns the sensory and motor innervation of visceral organs, provided by afferent and efferent fibers, respectively. By tracking trajectories of fascicles emerging from the sensory nodose ganglion (primarily afferent fascicles) and of fascicles by-passing the nodose (primarily efferent fascicles), we found spatial separation between the 2 groups, that persists throughout most of the cervical region; fascicles from the 2 clusters start merging in the lower cervical and are completely merged in the upper thoracic region (Figure 2B; Suppl. Figure S23). Along with the finding that organ-specific fascicular clusters form and merge at different levels in along the vagus, this suggests that, for purposes of selective neuromodulation, the level of placement of a bioelectronic device on the nerve is critical. The afferent-efferent separation involves large myelinated efferents that provide somatic motor innervation to the laryngeal muscles [10], but also small myelinated efferents (Figure 3C), that provide cholinergic, parasympathetic innervation to visceral organs, and even unmyelinated efferents, that may represent adrenergic sympathetic fibers (Figure 2B; Figure 3C; Suppl. Figure S13). Large, somatosensory, and smaller, viscerosensory, myelinated afferents also follow the afferent-efferent fascicular separation (Figure 3C; Suppl. Figure S13). Therefore, the afferent-efferent separation of fascicles may represent an organizing principle for both somatic and visceral fibers in the vagus throughout most of the cervical region, similar to the distinct topographic arrangement of some somatic peripheral nerves [30]. This finding suggests that, with regard to sensory-motor functions, both somatic and visceral, the cervical vagus is organized, at a large scale, in a “cable-like” manner (Figure 2A).

A third layer of neural organization in the vagus concerns the several anatomically- and functionally-distinct fiber types that comprise it [31]. Large myelinated efferents (Aα-type in the Erlanger-Gasser classification [32]) provide somatic innervation to laryngeal muscles, whereas smaller fibers (B-type) provide parasympathetic, cholinergic innervation to visceral organs. Large myelinated afferents (Aβ-type) provide somatic sensation to the pharyngeal and laryngeal mucosa, whereas smaller fibers (Aδ-type) provide visceral mechanical and chemical sensation to lungs and airways, vessels and the gastrointestinal tract. Unmyelinated (C-type) efferents mediate sympathetic innervation of visceral organs, e.g. [33], whereas C-type afferents provide nociception, temperature and chemical sensation, e.g. [34]. The human and swine vagus contain fibers of all these types. Historically, to obtain high resolution mapping of fiber types in the vagus, electron microscopy (EM) imaging has been used to visualize, classify and quantify single fibers based on their ultrastructural characteristics. To discriminate between afferent and efferent fibers, selective vagotomies are performed at different levels, causing selective loss of injured afferent or efferent axons, whose distributions are then compared to those in intact nerves. In those studies, fiber quantification is performed by manual annotation of EM images from randomly selected regions of the nerve; the number of fibers in the sampled area is then extrapolated to estimate the total number of fibers in the entire nerve [35]. The process is slow and cannot be used to resolve the full extent of fiber organization within and across fascicles in large nerves like the vagus in swine or humans, especially given the rich repertoire of fiber organization we describe here. While high-throughput segmentation algorithms of electron microscopy nerve images have been recently proposed , they only address the annotation part of the many bottlenecks that are involved in using EM imaging to resolve fiber organization. Even with these advanced techniques, segmentation accuracy leaves significant room for improvement.

To address these issues, we developed a quantitative anatomy pipeline for staining, imaging and automated annotation and quantification of single fibers. Antigens expressed by certain fiber types can be selectively targeted using a specific antibody tagged to a fluorophore [36]. Since antibody binding is highly sensitive and selective only to a particular antigen, multiple antibodies with different fluorophore wavelengths can be used to identify several antigens at the same time. For instance, in our study we used an IHC panel of antibodies against choline acetyltransferase (ChAT) (Suppl. Figure S17), neurofilament (NF) and myelin basic protein (MBP), which when they colocalize together to identify large myelinated efferent (MEff) fibers (Figure 3A). In the same panel, fibers that lack ChAT staining but are positive for NF and MBP were classified as myelinated afferents (MAff) and fibers that lack ChAT and MBP are classified as unmyelinated efferents (MEff). In our study we imaged the entire nerve and all fascicles at a resolution of 0.150 microns/pixel. At that resolution, individual axons as small as 0.3 μm diameter can be visualized and annotated. The IF technique in combination with the automated algorithm to efficiently analyze very large image sets provides unprecedented quantification of whole populations of fibers in large peripheral nerves. To the best of our knowledge, this is the first methodology that allows complete characterization of the main functional fiber types in the vagus, including small, unmyelinated fibers using light microscopy. ChAT+ fibers in previous reports were quantified using a DAB chromogen technique, at a relatively low power e.g. 20× [10]. In this work, we employed immunofluorescence (IF) to detect ChAT expression. The advantage of the IF technique is the ability to colocalize the ChAT expression with NF and MBP. Also, IF enabled us to visualize individual fibers at 100× magnification, accessing the subcellular localization of the ChAT, NF, and MBP in the same axon with high selectivity and sensitivity.

Small afferent fibers do not express NF in our stains (Suppl. Figure S18) and therefore could not be identified using that marker. We instead relied on an antibody against Nav1.8, a tetrodotoxin-resistant voltage-gated channel encoded by the SCN10A gene specifically expressed by small diameter sensory neurons in spinal and cranial nerves [37, 38], to identify clusters of unmyelinated afferents (Figure 3B; Suppl. Figure S10; Suppl.

Figure S11). Since non-myelinating Schwann cells in Remak bundles are known to encompass small unmyelinated fiber clusters [39, 40], we confirmed detection of C-afferent clusters by testing for co-localization with the S100 antibody expressed by Schwann cells (Figure 3B). In our study, Nav1.8+ fibers do not stain for MBP or NF, which is consistent with their expression in unmyelinated, nociceptor fibers but not myelinated, mechanoreceptor afferent fibers in the vagus [38]. Sizes and counts of Nav1.8+ fibers in our study are consistent with those of small, unmyelinated afferents in EM studies of the cervical vagus nerve in humans [41]. However, investigations directly comparing IHC to EM imaging will be needed for unequivocal confirmation that Nav1.8 is an accurate and precise marker of UAff fibers in the vagus nerve.

After testing different computer vision frameworks [42], we optimized the quantitative anatomy pipeline by segmenting nerve structures on micro-CT and IHC images using a mask-RCNN deep-learning architecture [43]. Deep-learning based algorithms have recently received attention in anatomically guided, medical image segmentation [44]. With regard to segmentation of anatomical features of nerves, deep-learning algorithms have been used on EM images [45], with regard to single fibers, and on ultrasound [46] and histological images [47], with regard to fascicles. To the best of our knowledge, this is the first use of convolutional neural networks, in particular mask-RCNN, on micro-CT and IHC data, to automatically segment and extract anatomical features at the fascicle and single fiber level. Until now, analysis of IHC data in nerves to segment single fibers has relied on manual or semi-automated processes, e.g. [48], which are inherently slow. Likewise, analysis of micro-CT data in nerves has used software-aided manual segmentation methods [49, 50]. After additional validation, similar pipelines to the ones described here may be useful in quantitative anatomical studies of peripheral nerves in health and disease, by improving efficiency and by minimizing sampling errors [51].

Using the pipeline, we were able to count, rather than estimate, the entirety of fibers in 8 vagus nerves (4 left, 4 right), at the cervical level. We classified each of those fibers in one of 4 types, including MEff, MAff, UEff and UAff (Table I; Suppl. Figure S12) and, with fiber diameter criteria, into additional functional sub-types (table I). The fiber counts we documented in the swine vagus are comparable to those reported in the, much less fascicular, ferret [52] and cat nerves [35]: MEff ~4% of all fibers in swine (4% in ferret), MAff ~8% (9% in cats and ferrets), UEff ~5% (8% in ferrets, 26% in cats), and UAff >80% (79% in ferrets, 54% in cats). Ours is the first quantification of the distribution of UEff fibers in the pig vagus. It is likely that many of the UEff fibers in the swine nerves are small, unmyelinated adrenergic fibers, even though we did not specifically stain for tyrosine hydroxylase (TH). In humans, recent evidence suggests the presence within the vagus nerve of hitchhiking branches projecting from the cervical sympathetic chain [53]. There is possibility that a percentage of UEff fibers are non-adrenergic non-cholinergic [54]. Our study is also the first to describe the complete arrangement of vagal UAff fibers across the entire vagus—or any large size nerve. UAff fibers occupy 5-10% of the nerve area on average and 1-28% of area in fascicles (Table I); accordingly, a recent EM study in the human cervical vagus estimated that UAff fibers occupy up to 18% of the nerve area [39]. In our study, UAff fibers are found in every fascicle; this means that even efferent fascicles have significant numbers of UAff fibers; given that efferent fascicles bypass the nodose ganglion, a portion of those fibers may represent peripheral axons of sensory cells outside of the nodose ganglion (e.g. jugular ganglion) or hitchhiking fibers from sensory fascicles. For all fiber types, the variation of fiber counts and occupied areas between fascicles is far greater than the variation between nerves or subjects (Table I), indicating that sampling from a subset of fascicles in a nerve may introduce estimation errors. Furthermore, fiber counts show interactions between fiber types at the fascicular and sub-fascicular level. Fascicles with high UEff fiber counts tend to have low MEff fiber counts, and vice versa (Figure 3D, a); because MAff and MEff fibers are found in separate fascicles, that also means UEff and MAff fibers tend to co-localize in the same fascicles (Figure 3D, b). Fiber interactions are observed at the sub-fascicular level, for instance myelinated fibers are frequently located in close vicinity of other

myelinated fibers, similar to MAff and UEff fibers (Figure 3D, c-e); UAff fibers also form clusters (Figure 3E, c), in agreement with what has been found in other peripheral nerves with C-type fibers [40]. The co-localization of certain afferent and efferent fiber types in the same fascicles and in the same sectors of fascicles suggests that the microscopic structure of the vagus may follow a “multiplexing” architecture, in which certain types of signals, from the same or different organs, are brought into close physical proximity as they are conveyed through the vagus; that organization pattern may have implications for the spatial arrangement of vagus sensory and motor neurons in the ganglia and the brainstem.

Following the example of classic studies that investigated how structure of autonomic nerves explains their function (e.g. [55]) we sought to determine whether the anatomical information gained in our studies could dictate strategies for spatially selective stimulation of the vagus. Selective VNS may provide a means to tailor stimulation to the individual nerve anatomy and engage the innervation of the desired organs with fewer off-target effects [3]. The use of multi-contact electrodes for current steering during nerve stimulation is an established method to deliver spatially selective stimulation, as it permits activation of sub-sets of fascicles or fibers. Such an approach has been followed in a rat model of VNS, in which reduction of blood pressure was attained without affecting heart rate and breathing rate [56] and has also been used in a sheep model of VNS, in which fascicular stimulation attained changes in breathing rate without affecting the heart rate [16]. Because surface electrodes are less invasive than intraneural probes, and therefore carry a smaller risk of injury to the vagus, and because most vagus fibers lie within less than 500 μm from the epineurium (Suppl. Figure S14), a cuff electrode may be a viable selective interface with the vagus. In a simplified model of the spatial overlap between fascicles and contact generated electrical fields, a cuff with 8 contacts, placed on a helical substrate circumferentially around the nerve, provides close to maximal efficacy, with similar selectivity as configurations with more contacts (Suppl. Figure S19B). This configuration is compatible with the fascicular anatomy of the human vagus nerve (Suppl. S19C).

Delivering stimulation through different cuff contacts results in differential engagement of fibers innervating the larynx, the lungs and the heart, as demonstrated by the different patterns of physiological and evoked potential responses (Figure 4B). Correlations between physiological and corresponding nerve fiber responses are seen in the recruitment curves, which are also different among different contacts (Figure 4F). This indicates that the differences among contacts in the stimulation intensity thresholds arise because of differential activation of separate fiber populations. The different radial distributions of thresholds for e.g. cardiac vs. respiratory responses indicates that between-contact differences arise because of differences in the underlying fiber distribution, rather than other factors that affect one side of the nerve or the interface (e.g. thicker epineurium or looser placement of the cuff). The fact that we observe evoked compound action potentials comprised of only fast and slow A-fiber components may be related to the overrepresentation of large myelinated fibers in terms of nerve area covered (Table I) or to the stimulus intensities used in this study, that may have been below the activation thresholds for smaller fibers. Asymmetrical engagement physiological responses, related to cough reflex, was also observed in longitudinal survival experiments conducted over a period of 3 weeks after the cuff implantation, in a first report of a chronic vagus implant in swine (Suppl. Figure S20). Cough and throat pain is a common off-target effect of cervical VNS and our findings indicate that its magnitude could in principle be reduced by selective VNS.

The angular separation between the cardiac-, lung- and larynx-selective contacts (Figure 4F) is likely to reflect the underlying anatomical arrangement of fascicles contributing to cardiac, bronchopulmonary and laryngeal branches (Figure 1), even though, in this study, we did not co-register the exact contact locations with the specific nerve anatomy. In addition, the angular separation between the fast-fiber-selective contacts and slow-fiber-selective contacts (90° counter-clockwise, Figure 4H) is in agreement with that between contacts eliciting corresponding physiological functions, i.e., fast-fiber-mediated laryngeal EMG and slow-fiber-mediated

changes in breathing rate (also 90° counter-clockwise, Figure 4F). Even though physiological and eCAP responses were registered in almost all animals, we did not align eCAP responses by the contact with the minimum heart rate threshold, but to the contact with the maximum fast fiber amplitude. eCAPs are recorded through a second multi-contact cuff (Suppl. Figure S21), placed at a distance of at least 5 cm from the stimulating cuff and, over that distance, fascicles merge or split and their radial location in the trunk changes significantly (Suppl. Video 1). For that reason, the spatial arrangement of fascicles at the stimulating cuff, assessed through physiological thresholds, is different than the arrangement at the recording cuff, and aligning the 2 response patterns would be unlikely to produce interpretable results.

The selectivity profile of a multi-contact nerve interface depends on the spatial relationship between the contacts and the underlying nerve anatomy and will naturally be different between subjects. Resolving the selectivity profile on a single subject basis requires semi-real time “nerve mapping” methods. Large-scale fascicular structure of the swine vagus has been visualized with noninvasive, high resolution ultrasound imaging [24] or with electrical impedance tomography of nerve activity [57, 58]. Our results show that functional nerve mapping can be also performed by quantifying physiological and/or nerve fiber responses delivered through different contacts and visualizing their spatial distributions around the nerve (Figure 4D, E). Such physiological responses or fiber responses to stimulation can be registered and processed in real-time in humans or experimental animals [59].

Methods

Animal surgeries

The effects of VNS on physiological and neural response were examined in male pigs (Yucatan; n=13, ~50kg; Yorkshire, n=1, ~30 kg). All of the animal protocols and surgical procedures were reviewed and approved by the animal care and use committee of Feinstein Institutes for Medical Research and New York Medical College.

Anesthesia: For a 12-hour period before surgery, the animals were maintained on a no-food and no-fluid regimen (NPO). On the day of surgery, the animals were weighed and sedated with mixture of Ketamine (10-20 mg/kg) and Xylazine (2.2 mg/kg) or Telazol (2-4 mg/kg). Propofol (4-6 mg/kg, i.v.) was used to induce anesthesia, and following intubation, the anesthesia will be maintained with isoflurane (1.5-3%, ventilation). Mechanical ventilation will be provided and might be turned off to measure the breathing change during VN stimulation. Animals were placed on a table in a supine position with normal body temperature between maintained between 38°C and 39°C using a heated blanket and/or a hot air warmer and monitored with a rectal probe thermometer. Blood pressure and blood oxygen level were monitored with a BP cuff and a pulse oximeter sensor. The depth of anesthesia was monitored by assessing heart rate, blood pressure, respiration, and mandibular jaw tone. All surgeries were performed using sterile techniques.

For survival surgeries, a fentanyl patch (25-50 mcg/hr) and buprenorphine (0.01 mg/kg s.q.) were provided to the animal at the end of surgery to alleviate post-operative pain. After gradually weaning off the ventilator and extubated and when physiological signs returned to normal, animals were returned to the home cage and were monitored 3 times/day for 72 hours. Cefazolin (25 mg/kg p.o.) was given for 5 days. Carprofen (2-5 mg/kg, s.q.) was administered when the animal showed signs of pain. Animals were allowed 10 days for full recovery before any tests were performed.

Cervical vagus nerve and laryngeal muscle implants

Under the surgical level of anesthesia, a 4-5 cm long incision was cut down to the subcutaneous tissue on the right or left cervical region of the neck, 2 cm lateral to the midline. Subcutaneous tissues were dissected and retracted to expose the underlying muscle layers. The sternomastoid muscle was bluntly separated and retracted laterally away from the surgical field. The carotid sheath was exposed and the vagus nerve was identified and isolated away from the carotid artery. One or two helical cuff electrodes (CorTec, Germany) were placed on the rostral (around 2cm to nodose) and/or caudal sites with a distance of 4 to 5 cm after isolating the underlying 2 cm long section for each electrode. The helical cuff included 8 contacts (0.5mmX0.5mm) evenly distributed (1mm between two contacts) around the circumference and 2 ring-shaped (0.5mmX7.4mm) return contacts. The middle portion, between the two isolated sites was left intact within the carotid bundle to minimize the extent of surgical manipulation and trauma to the nerve. For laryngeal muscle recording, after the hyoid bone was blunt dissected, Telfon-insulated single or multi-stranded stainless-steel wires were de-insulated at the tip about 1 mm, and inserted in thyroarytenoid (TA) of laryngeal muscle with a needle. For survival surgery, the incision was closed, the leads and connectors of the implanted cuff electrodes and EMG electrodes are tunneled from the surgical field in the neck area to the back of the neck subcutaneously and then to the top of the skull, where they are externalized. Several stainless-steel skull screws are implanted in the exposed area of the skull by drilling small burr holes. The connectors and the anchoring screws are secured with dental acrylic, and then a titanium casing will be attached around and secured to the skull around the connector for protection of the implants.

Physiology experiments

Breathing rate: Breathing was monitored by using a respiratory belt transducer (TN1132/ST), which was placed around the belly or chest and connected to a bridge amplifier (FE221, ADI). The change of the belt pressure with breathing represented the breathing cycle and was used to derive the breathing rate. The mechanical ventilator was turned off when measuring the effects of vagus nerve stimulation on breathing.

ECG: The skin around the wrist was shaved and conductive gel was applied to patch electrodes which were subsequently adhered to the skin, ECG was recorded using a 3-lead patch electrode configuration and amplified using a commercial octal bio-amplifier (FE238, ADI).

Heart blood pressure: Ultrasonic guidance (H8018QE and Vivid IQ v203 4D) was used to pass a 19 G angiographic needle through the skin at a 60-degree angle to the target vessel. Once blood backflow was detected, a soft guidewire (0.035 inches) was introduced into the vessel. A 5-Fr micro manometer-tipped catheter (SPR-751, Millar Inc) was advanced into the aorta or right ventricle, and pressure was recorded continuously after amplification (FE228 ADInstruments). The catheter locations were confirmed by verifying the characteristic phasic blood pressure waveforms corresponding to different placements.

All physiological signals were first digitized and then acquired at 1 kHz (PowerLab 16/35, ADI) and then visualized using LabChart (ADInstruments Inc).

Neural signal and EMGs were sent to the data acquisition system through a headstage (RHS 32, Intan Tech). Signals were digitized at a sampling frequency of 30 ks/s with an acquisition system (Intan 128 recording/stimulating, Intan Tech).

Vagus nerve stimulation and physiological data analysis

Physiological thresholds: Biphasic stimulus pulses were delivered through an isolated constant current stimulator (STG4008, Multichannel Systems). Physiological threshold (PT) was detected from stimulus trains of 10 s durations (30 Hz, pulse width 200 μs). There was at least 30 s long duration between successive trains to ensure that physiological measurements had reached a steady state before a new train was delivered. We define PT as the lowest stimulation intensity to induce 5-10% drop in HR, and ~50% drop in BR as the thresholds for HR and BR, respectively. In awake animals we tested PT of cough reflex, which is the lowest stimulation intensity to induce coughing. The threshold of EMG was the lowest intensity to induce a visible response. The thresholds for each of the eight contacts were tested in a random order.

Evoked compound action potential (eCAP): After removing the DC component (<1 Hz) from recordings, evoked compound action potentials (eCAP) from the vagus nerve were averaged across all of the individual stimulus pulses within each train. The responses (peak-to-peak) from eCAP within predefined time window were classified into different fibers based on the conduction speed. Given the distance between recording and stimulation electrode, ~45-60 mm, the first peak latency within 1.5 ms (conduction speed, >33 m/s) was classified as a fast fiber response, consistent with activation of large, myelinated A-type fibers; the late peak after 2 ms (conduction speed, <20 m/s) was classified as slow fiber response, consistent with activation of smaller, myelinated fibers (Aδ- and B-type). In most of the recordings, EMG contamination observed in eCAP recordings could be blocked by Vecuronium. Long latency C-fiber response was not observed in our tests. The eCAP responses (peak-to-peak amplitude) from eight contacts on the second cuff were recorded simultaneously while stimulating each of the eight contacts; however, because of the high degree of similarity between individual eCAP traces elicited from the same stimulated contact (Suppl. Figure S21), eCAP traces were analyzed after being averaged across the recording contacts.

Recruitment map and population responses: The responses from laryngeal muscle (peak-to-peak EMG amplitude), breathing rate change and mean eCAPs responses (of 8 contacts) of different fibers were characterized to inform recruitment maps during increasing stimulation intensity across 8 stimulating contacts.

To characterize the spatial selectivity of the 8-contact cuff, PTs and eCAPs from each contact were plotted on a polar-plot with mean direction and resultant vector length. To show the spatial selectivity across animals and compare difference between physiological responses, we aligned the lowest thresholds of HR on the 12 o'clock position from all animals, and then PTs of BR and EMG was aligned to the HR. Then the PTs were normalized between the lowest (to 0) and highest (to 1) to give the population (mean+/- SE) across animals. Similarly, we first aligned the highest responses (eCAP of peak-to-peak amplitude) of fast fiber to 12 o'clock position, and then we get the population eCAPs (mean+/- SE) across all animals, and finally the population response from slow fiber eCAPs were alighted to the fast response for each pig and averaged across animals (mean+/- SE). ANOVA was used to test the spatial selectivity across contacts (anova1, *$p<0.05$).

Euthanasia and surgical dissection nerve samples for micro-computed tomography

At the end of the study, the swine was euthanized with a solution (Euthasol) (A dosage of 1 ml/10 pounds BW, i.v.). Euthanasia solution (Euthasol) was injected intravenously. Death was confirmed using the ECG signal and the arterial blood pressure signal. Absence of a pulse in both signals confirmed cardiac death. After euthanasia, both the left and right cervical vagus nerve were dissected from above the nodose ganglion to the end of the thoracic vagus; during that time, nerve branches, still attached to the nerve trunk, were isolated using blunt dissection up to the respective end organ (heart, lung or larynx). A fine suture loop (6-0) was placed on the epineurium of each branch, close to its emergence from the trunk, as a label. The samples were fixed in 10% formalin for 24 hours, then transferred to Lugol's solution (Sigma, L6146) for five days to achieve optimal fascicular contrast for the micro-CT. Nerve samples were wrapped in a less dense material such as saran wrap and mounted in position on a vertical sample holder tube. The samples were scanned using Bruker micro-CT skyscan 1172 with a voxel size of 6 μm resolution. Volume rendering was done using Bruker CTvox v3.3.1 to obtain a 3D reconstructed view of the nerve (Suppl. Figure S2-S4).

Segmentation and tracking of fascicles in micro-CT data

The automated fascicle tracing approach consists of two stages: segmentation and tracking. Instance segmentation on micro-CT images was performed using the Matlab Deep Learning toolbox, Mask R-CNN model implementation (Mathworks, Inc.). The mask R-CNN model comes pretrained based on the COCO image dataset and transfer learning was applied by freezing the Resnet50-coco backbone during training which forces the model to utilize the existing COCO features from the Resnet50 subnetwork while updating the weights of the region proposal network and mask head. Since micro-CT images are significantly different than COCO images (grayscale intensity images as opposed to color photographs, content is at a much smaller spatial scale), to achieve adequate performance, 80% of images that were annotated from the initial nerve needed to be included in the training data. Once the fascicle detection mask R-CNN model was trained (stage 1), it was updated for each new nerve sample with fewer annotated slices (stage 2); we annotated 1 out of every 50 micro-CT slices on subsequent nerves. The annotated images included three categories: fascicle, false alarm on nerve, and false alarm off nerve. The false alarm classes were created by storing the segmentation results that didn't overlap with the ground truth annotations and then subcategorizing them based on the average pixel intensity within the detection masks. We chose an initial learning rate during training for each stage, λ_0, to $1.2 * 10^{-5}$, that was decreasing with each epoch, based on the formula $\lambda=\lambda_0/(1+$

τ(epoch-1)), where *τ* is a decay rate of 0.01. The model was trained for 18 epochs resulting in training iterations which is on par with the number of training iterations used to train the original Mask R-CNN model [60]; stochastic gradient descent with momentum was used to update the network weights with a momentum of 0.9 and a minibatch size of 1. We chose a mask RCNN model as our detector because it performs well on the detection task and can readily be updated in individual animals if necessary. Shape-based, pixel-based, and texture-based features were extracted for each detected fascicular cross-section. Shape-based features consist of the centroid, circularity, eccentricity, irregularity, area, orientation, major and minor axes lengths, solidity, and the weighted centroid. Pixel-based features consisted of the mean pixel intensity and central moments like variance, skewness, and kurtosis. Texture-based features were derived from the gray-scale co-occurrence matrix and include contrast, correlation, energy, and homogeneity. A minimum area constraint of 120 pixels was imposed based on the smallest area in the annotated data.

After the detected fascicular cross-sections for each slice of the micro-CT data were determined, the structure of the nerve was estimated by tracking the fascicular cross-sections longitudinally. The tracker filters and structures the detections to construct a graph that captures properties of the fascicular cross-sections (shape and texture metrics) at each node and encodes branching and merging via the graph edges. We used a windowed, density-based-clustering approach. The distances between the detected fascicles within the micro-CT slice window were computed as *1 - J*, where *J* is the Jaccard similarity (a.k.a. intersection over union). DBSCAN was sued to cluster the detected fascicular cross-sections at each window position, with a minimum of 3 samples per cluster and an epsilon neighborhood of 0.6. A track was extended if more than 2/3 of the detections are the same between the adjacent window positions. Any detections that are not included in a track was discarded, except for detections that correspond to manual annotations. Once this step was completed, a post-processing algorithm was run on the tracks to connect broken segments that result from missed detections and detect branching and merging events. Individual fascicles contributing to the different vagal branches were manually identified at the branching points (Suppl. Figure S2-S4). The tracked fascicle trajectories were then color coded from the caudal end of the branching point to the rostral end of the nodose ganglion (Figure 1).

Immunohistochemistry

Cross-section of the vagus nerve at 5 µm thickness was obtained through paraffin sectioning. Sections were stained for myelin basic protein (MBP), neurofilament (NF), choline acetyltransferase (ChAT) and Nav1.8 using standard IHC protocol [61] to identify the number and distribution of the myelinated and non-myelinated fibers inside different fascicles. Briefly, sections were subjected to deparaffinization procedure using xylene and ethanol rinse and then washed with distilled water for 10 min. Antigen retrieval was performed by briefly subjecting the samples to 1 x citrate buffer to unmask the antigens. Sections were rinsed with 1x Tris-buffered saline and subjected to 1 hour of blocking step using one normal goat serum. Sections were incubated with anti-Neurofilament (1:500, Abcam AB8135), anti- Myelin basic protein (1:500, Abcam AB7349) and either anti-ChAT (Millipore Sigma, AB144P) (“efferent IHC panel”) or SCN10A Monoclonal Antibody (Nav1.8, MA5-27663 Fisher) (“afferent IHC panel”), overnight at 4 °C in a shaking humidifier. The following day, sections were rinsed and incubated with the secondary antibody for two hours at room temperature. Slides were then rinsed thoroughly with TBS buffer three times, and cover glass was mounted on the sides with the fluoromount (Vector labs, H-1700). The slides were then imaged using ZEISS LSM 900, confocal laser scanning microscope, and BZ-X800 all-in-one fluorescence microscope at 100x magnification.

Fiber segmentation and feature extraction

We designed a set of algorithms and a data pipeline to segment and extract nerve, fascicle and single-axon level features from IHC images of the vagus. First, we developed a fiber segmentation and feature extraction algorithm by combining standard computer vision methods with statistical modeling and geometrical manipulations, including Gaussian mixture models and Voronoi tessellation, and achieved a single-axon detection accuracy of 82% and myelination classification accuracy of 89% [42].

To improve the detection accuracy, we further trained a Mask R-CNN deep convolutional neural network on axon instance segmentation. The model was pretrained on the COCO Instance Segmentation task [62]. We generated training images by first annotating fibers using the more standard algorithm, followed by manual correction of 80 fascicles, done in an ordinary image editing software. We estimated that pre-annotating using the original algorithm reduced the time of correction by four times compared to manual annotation from scratch.

Fiber Detection

Neurofilament: To detect neurofilament positive pixels, we empirically selected a threshold brightness in the neurofilament color channel (154 out of 256) above which pixels were classified as positive. We further discovered connected components of such pixels to arrive at blobs of neurofilament. Blobs containing less than 10 pixels were excluded as noise. The remaining blobs were broken divided into individual fibers by fitting Gaussian mixture model on them of different number of Gaussian distributions (i.e. number of fibers) and then selecting the best fit determining the amount and location of enclosed axons.

Myelin: Myelin positive pixels were detected using the same technique as described previously [42]. Briefly, myelin channel pixels surrounding each detected neurofilament positive axon were analyzed. Pixels were classified as myelin positive when their brightness reached 128 out of 256. First, the outside pixel shell of neurofilament positive fibers were taken and neighboring pixels were recursively checked (for a maximum of 5 recursive steps) for myelin positive pixels. If more than 30% of fiber neighboring pixels were found to be myelin positive, the said fiber was classified as myelinated.

ChAT: Similar to Neurofilament and myelin pixel classification, we empirically selected a brightness threshold, applied to the chat color channel, of 131 out of 256. ChAT positive pixels overlapping myelinated axons were counted separately for each fiber and if more than 5% of pixels were found to be chat positive, we regarded the fiber as chat positive.

The final set of segmentations was performed by the combination of the standard computer vision and deep learning algorithms: we let Mask R-CNN detect axons first, then opted for traditional methods to detect and divide overlapping neurofilament blobs that were ignored by the deep learning model. This combination achieved a fiber detection accuracy of 96% [63]

After the instance segmentation of neurofilament and the assignment of myelin to detected fibers, we extracted a set of features for each axon. These features include the longer and shorter diameters, the perimeter, and area of the fiber, in addition to the thickness of the myelin, and the polar coordinates of the fiber relative to the center of mass of the enclosing fascicle.

We manually annotated nerve cross-sections on the fascicle level to derive polar coordinates of fascicles and their distance from the epineurium. Moreover, we extracted fascicle-level features including the perimeter of the perineurium, the area of the fascicle enclosed by the perineurium, and the total count and area of each fiber type within a fascicle.

Nav1.8: To generate ground truth data for the deep learning instance segmentation network, we performed manual annotation of NAV1.8 stained images to determine the density of C fibers within bundles given the area of the enclosing bundle. Due to the low resolution of light microscopy at the range of 1 µm, we used Airyscan equipped super high resolution confocal microscope captured laser microscopy images of parts of fascicles, from which single NAV1.8 positive C fibers can be distinguished (Suppl. Figure S11, a). These high resolution images were manually annotated bundle-by-bundle to amass counts of fibers within more than 300 bundles extracted from two animals and four different fascicles. To predict number of NAV1.8 positive C fibers from lower resolution light microscopy images (Suppl. Figure S11, c) a linear regression model was fit on the C fiber counts given the area of the bundle (r^2 = XY) (Suppl. Figure S11, d). We subsequently employed the linear regression model to estimate the number of NAV1.8 positive C fibers in clouds of NAV1.8 stains, detected as bundles, in light microscopy images (Suppl. Figure S11, e). As the linear regression model estimates are real numbers, we round those numbers to the closest integer for each detected bundle to get actual counts.

All images are preprocessed before the segmentation to enhance contrast and to remove noise. Myelin-neurofilament-ChAT stained images were first adjusted by adaptive histogram equalization (dividing each fascicle image into a 32-by-32 grid), then color clipped by defining upper and lower threshold of the clip for separately each cross section manually. The thresholds for each cross-section and channel were selected to remove background noise and to render the stains close to binary (distinct foreground and background), which removed the brightness variance between cross-sections allowing us to use the same parameters for all cross-sections in the subsequent segmentation process. Myelin-neurofilament-NAV1.8 images were not processed by adaptive histogram equalization, but were color clipped as described above. In the subsequent segmentation process, we ignore all individual neurofilament and NAV1.8 blobs that are smaller than 0.225 μm^2, which we found to be background noise rather than actual fibers.

Data analysis

Once we detected and localized fibers and fascicles, and further extracted features from them, we performed subsequent analysis to map the distribution of different fiber types within-fascicle, and within the whole nerve.

We calculated within-fascicle counts and areas of the four fiber types, namely, myelinated efferents (MEff), myelinated afferents (MAff), unmyelinated efferents (UEff) and unmyelinated afferents (UAff). The per-fascicle counts are either presented in their absolute values (Figure 3A, I-L) or as percentages normalized by the total fiber count per fascicle (Figure 3C).

For each fiber type we estimated the ratio of its neighboring fiber types in a 15 µm radius (Figure 3E, c). For each fiber in every fascicle at the mid-cervical level, we captured its neighboring fibers using k-nearest neighbors, then filtered out the ones outside of the 15 µm radius of the fiber. We accumulated the counts of neighboring fiber types for each center fiber type; normalized by the total count of neighbors we calculated the overall ratio of a fibers a given type being in the vicinity of a given fiber type. To further describe the tendency of different fiber types to share space, we compared their total numbers in each fascicle (Figure 3D, a & b). Within-fascicle mixing was analyzed by splitting each mid-cervical fascicle into a grid of 30-by-30 µm non-overlapping spatial sectors, establish the fiber counts by type in the sectors, then finally count the number of sectors of a certain composition and represent the propensity of two fiber types to share a space of 30-µm-width fascicle area by showing a 2D histogram of the distribution of compositions of the two fiber types (Figure 3E, a & b)

To examine distribution of fiber types within the nerve, we measured the percentage of a fiber type being positioned in fascicles inside rings of 100-µm width at different distances from the epineurium. We show the

overall distribution of fiber types as the function of epineurium distance combining data extracted from nerves of different animals at the mid-cervical level (Suppl. Figure S14, A). We also present the same information for individual nerves as cumulative distributions (Suppl. Figure S15). We grouped fascicles according to their effective diameter into 50 -μm bins and measured the percent area occupied by each fiber type within each fascicle normalized by the area of the fascicle. We then computed the average and standard deviation of such fiber type percentages per effective diameter bin (Suppl. Figure S14, B).

As we manually annotated single fibers of MEff, MAff, UEff and UAff to generate ground truth data for our instance segmentation and NAV1.8 positive C-fiber counting model, we had access to accurate single-fiber features. To gauge the size of the different fiber types, we measured the effective diameter of the manually annotated single fibers of each type and presented their distribution (Suppl. Figure S12).

Acknowledgments

This work was supported by a grant from United Therapeutics Corp. to SZ and by an NIH-SPARC grant to LM (1OT2OD026539). The authors would like to acknowledge Drs. Betty Diamond, Loren Rieth, Thomas Coleman, Valentin Pavlov and Sangeeta Chavan for helpful discussions.

Author contributions

NJ, VT and WS designed experiments, performed experiments and collected data, analyzed data, interpreted data and wrote the paper. AV and TL analyzed data, interpreted data and wrote the paper. JNT and KQ performed experiments and collected data. IM, YCC, MR, AD, AA, JA, Anna Vikatos, UA and Anil Vegesna collected and analyzed data. ZN, BTV, KJT, YA, TDC interpreted data and wrote the paper. LM, MFB and SCL performed experiments and collected data, interpreted data and wrote the paper. TPZ designed experiments, analyzed data, interpreted data and wrote the paper. SZ designed experiments, performed experiments and collected data, analyzed data, interpreted data, wrote the paper and managed the project. SZ and LM acquired funding.

References

1. Stakenborg, N., et al., *Comparison between the cervical and abdominal vagus nerves in mice, pigs, and humans.* Neurogastroenterol Motil, 2020. **32**(9): p. e13889.
2. Pelot, N.A., et al., *Quantified Morphology of the Cervical and Subdiaphragmatic Vagus Nerves of Human, Pig, and Rat.* Front Neurosci, 2020. **14**: p. 601479.
3. Thompson, N., S. Mastitskaya, and D. Holder, *Avoiding off-target effects in electrical stimulation of the cervical vagus nerve: Neuroanatomical tracing techniques to study fascicular anatomy of the vagus nerve.* J Neurosci Methods, 2019. **325**: p. 108325.
4. Kenny, B.J. and B. Bordoni, *Neuroanatomy, Cranial Nerve 10 (Vagus Nerve)*, in *StatPearls*. 2021: Treasure Island (FL).
5. De Ferrari, G.M., et al., *Long-term vagal stimulation for heart failure: Eighteen month results from the NEural Cardiac TherApy foR Heart Failure (NECTAR-HF) trial.* Int J Cardiol, 2017. **244**: p. 229-234.
6. Mikami, Y., et al., *Vagus nerve-mediated intestinal immune regulation: therapeutic implications of inflammatory bowel diseases.* Int Immunol, 2022. **34**(2): p. 97-106.
7. Koopman, F.A., et al., *Vagus nerve stimulation inhibits cytokine production and attenuates disease severity in rheumatoid arthritis.* Proc Natl Acad Sci U S A, 2016. **113**(29): p. 8284-9.
8. Giordano, F., et al., *Vagus nerve stimulation: Surgical technique of implantation and revision and related morbidity.* Epilepsia, 2017. **58 Suppl 1**: p. 85-90.
9. Nicolai, E.N., et al., *Sources of off-target effects of vagus nerve stimulation using the helical clinical lead in domestic pigs.* J Neural Eng, 2020. **17**(4): p. 046017.
10. Settell, M.L., et al., *Functional vagotopy in the cervical vagus nerve of the domestic pig: implications for the study of vagus nerve stimulation.* J Neural Eng, 2020. **17**(2): p. 026022.
11. Hoffman, H.H. and H.N. Schnitzlein, *The numbers of nerve fibers in the vagus nerve of man.* Anat Rec, 1961. **139**: p. 429-35.
12. Pelot, N.A. and W.M. Grill, *Effects of vagal neuromodulation on feeding behavior.* Brain Res, 2018. **1693**(Pt B): p. 180-187.
13. Gold, M.R., et al., *Vagus Nerve Stimulation for the Treatment of Heart Failure: The INOVATE-HF Trial.* J Am Coll Cardiol, 2016. **68**(2): p. 149-58.
14. Musselman, E.D., N.A. Pelot, and W.M. Grill, *Empirically Based Guidelines for Selecting Vagus Nerve Stimulation Parameters in Epilepsy and Heart Failure.* Cold Spring Harb Perspect Med, 2019. **9**(7).
15. Fitchett, A., S. Mastitskaya, and K. Aristovich, *Selective Neuromodulation of the Vagus Nerve.* Front Neurosci, 2021. **15**: p. 685872.
16. Aristovich, K., et al., *Model-based geometrical optimisation and in vivo validation of a spatially selective multielectrode cuff array for vagus nerve neuromodulation.* J Neurosci Methods, 2021. **352**: p. 109079.
17. Erman, A.B., et al., *Disorders of cranial nerves IX and X.* Semin Neurol, 2009. **29**(1): p. 85-92.
18. Yuan, H. and S.D. Silberstein, *Vagus Nerve and Vagus Nerve Stimulation, a Comprehensive Review: Part I.* Headache, 2016. **56**(1): p. 71-8.
19. Weijs, T.J., et al., *Topography and extent of pulmonary vagus nerve supply with respect to transthoracic oesophagectomy.* J Anat, 2015. **227**(4): p. 431-9.
20. Gunter, C., J. Delbeke, and M. Ortiz-Catalan, *Safety of long-term electrical peripheral nerve stimulation: review of the state of the art.* J NeuroEng Rehab, 2019. **16**(13).
21. Sahyouni, R., et al., *Functional and Histological Effects of Chronic Neural Electrode Implantation.* Laryngoscope Investig Otolaryngol, 2017. **2**(2): p. 80-93.
22. Ahmed, U., et al., *Implant- and anesthesia-related factors affecting cardiopulmonary threshold intensities for vagus nerve stimulation.* J Neural Eng, 2021. **18**(4).
23. Peclin, P. and J. Rozman, *Alternative paradigm of selective vagus nerve stimulation tested on an isolated porcine vagus nerve.* ScientificWorldJournal, 2014. **2014**: p. 310283.
24. Settell, M.L., et al., *In vivo Visualization of Pig Vagus Nerve "Vagotopy" Using Ultrasound.* Front Neurosci, 2021. **15**: p. 676680.
25. Hammer, N., et al., *Human vagus nerve branching in the cervical region.* PLoS One, 2015. **10**(2): p. e0118006.
26. Zafeiropoulos, S., et al., *Autonomic Neuromodulation for Atrial Fibrillation Following Cardiac Surgery: JACC Review Topic of the Week.* J Am Coll Cardiol, 2022. **79**(7): p. 682-694.
27. Geis, G.S. and R.D. Wurster, *Cardiac responses during stimulation of the dorsal motor nucleus and nucleus ambiguus in the cat.* Circ Res, 1980. **46**(5): p. 606-11.
28. Broussard, D.L. and S.M. Altschuler, *Brainstem viscerotopic organization of afferents and efferents involved in the control of swallowing.* Am J Med, 2000. **108 Suppl 4a**: p. 79S-86S.
29. Huang, X.F., I. Tork, and G. Paxinos, *Dorsal motor nucleus of the vagus nerve: a cyto- and chemoarchitectonic study in the human.* J Comp Neurol, 1993. **330**(2): p. 158-82.

30. Agostoni, E., et al., *Functional and histological studies of the vagus nerve and its branches to the heart, lungs and abdominal viscera in the cat.* J Physiol, 1957. **135**(1): p. 182-205.
31. Kenny, B.J. and B. Bordoni, *Neuroanatomy, Cranial Nerve 10 (Vagus Nerve)*, in *StatPearls*. 2022: Treasure Island (FL).
32. Erlanger, J., H.S. Gasser, and G.H. Bishop, *The compound nature of the action current of nerve as disclosed by the cathode ray oscillograph.* Am J Physiol, 1924. **70**: p. 624-666.
33. Seki, A., et al., *Sympathetic nerve fibers in human cervical and thoracic vagus nerves.* Heart Rhythm, 2014. **11**(8): p. 1411-7.
34. Kollarik, M., F. Ru, and M. Brozmanova, *Vagal afferent nerves with the properties of nociceptors.* Auton Neurosci, 2010. **153**(1-2): p. 12-20.
35. Mei, N., M. Condamin, and A. Boyer, *The composition of the vagus nerve of the cat.* Cell Tissue Res, 1980. **209**(3): p. 423-31.
36. Schemann, M., et al., *Identification of cholinergic neurons in enteric nervous system by antibodies against choline acetyltransferase.* Am J Physiol, 1993. **265**(5 Pt 1): p. G1005-9.
37. Akopian, A.N., L. Sivilotti, and J.N. Wood, *A tetrodotoxin-resistant voltage-gated sodium channel expressed by sensory neurons.* Nature, 1996. **379**(6562): p. 257-62.
38. Gautron, L., et al., *Genetic tracing of Nav1.8-expressing vagal afferents in the mouse.* J Comp Neurol, 2011. **519**(15): p. 3085-101.
39. Havton, L.A., et al., *Human organ donor-derived vagus nerve biopsies allow for well-preserved ultrastructure and high-resolution mapping of myelinated and unmyelinated fibers.* Sci Rep, 2021. **11**(1): p. 23831.
40. Murinson, B.B. and J.W. Griffin, *C-fiber structure varies with location in peripheral nerve.* J Neuropathol Exp Neurol, 2004. **63**(3): p. 246-54.
41. Gabella, G. and H.L. Pease, *Number of axons in the abdominal vagus of the rat.* Brain Res, 1973. **58**(2): p. 465-9.
42. Toth, V., et al., *Single-axon level automatic segmentation and feature extraction from immuhistochemical images of peripheral nerves.* Annu Int Conf IEEE Eng Med Biol Soc, 2020. **2020**: p. 1859-1862.
43. He, K., et al., *Mask R-CNN.* IEEE Trans Pattern Anal Mach Intell, 2020. **42**(2): p. 386-397.
44. Liu, L., et al., *Anatomy-aided deep learning for medical image segmentation: a review.* Phys Med Biol, 2021. **66**(11).
45. Plebani, E., et al., *High-throughput segmentation of unmyelinated axons by deep learning.* Sci Rep, 2022. **12**(1): p. 1198.
46. Horng, M.H., et al., *DeepNerve: A New Convolutional Neural Network for the Localization and Segmentation of the Median Nerve in Ultrasound Image Sequences.* Ultrasound Med Biol, 2020. **46**(9): p. 2439-2452.
47. Tovbis, D., et al., *Automatic three-dimensional reconstruction of fascicles in peripheral nerves from histological images.* PLoS One, 2020. **15**(5): p. e0233028.
48. Sun, K., et al., *Three-dimensional reconstruction and visualization of the median nerve from serial tissue sections.* Microsurgery, 2009. **29**(7): p. 573-7.
49. Prats-Galino, A., et al., *3D reconstruction of peripheral nerves from optical projection tomography images: A method for studying fascicular interconnections and intraneural plexuses.* Clin Anat, 2018. **31**(3): p. 424-431.
50. Thompson, N., et al., *MicroCT optimisation for imaging fascicular anatomy in peripheral nerves.* J Neurosci Methods, 2020. **338**: p. 108652.
51. Mayhew, T.M., *Efficient and unbiased sampling of nerve fibers for estimating fiber number and size*, in *Quantitative and Qualitative Microscopy*, M.P. Conn, Editor. 1990, Academic Press: NY. p. 172-187.
52. Asala, S.A. and A.J. Bower, *An electron microscope study of vagus nerve composition in the ferret.* Anat Embryol (Berl), 1986. **175**(2): p. 247-53.
53. Verlinden, T.J., et al., *Morphology of the human cervical vagus nerve: implications for vagus nerve stimulation treatment.* Acta Neurol Scand, 2016. **133**(3): p. 173-82.
54. Moffatt, J.D., B. Dumsday, and J.R. McLean, *Characterization of non-adrenergic, non-cholinergic inhibitory responses of the isolated guinea-pig trachea: differences between pre- and post-ganglionic nerve stimulation.* Br J Pharmacol, 1999. **128**(2): p. 458-64.
55. Armour, J.A. and W.C. Randall, *Functional anatomy of canine cardiac nerves.* Acta Anat (Basel), 1975. **91**(4): p. 510-28.
56. Gierthmuehlen, M., et al., *Haemodynamic Responses to Selective Vagal Nerve Stimulation under Enalapril Medication in Rats.* PLoS One, 2016. **11**(1): p. e0147045.
57. Aristovich, K., et al., *Imaging fast neural traffic at fascicular level with electrical impedance tomography: proof of principle in rat sciatic nerve.* J Neural Eng, 2018. **15**(5): p. 056025.
58. Ravagli, E., et al., *Optimization of the electrode drive pattern for imaging fascicular compound action potentials in peripheral nerve with fast neural electrical impedance tomography.* Physiol Meas, 2019. **40**(11): p. 115007.
59. Chang, Y.C., et al., *Quantitative estimation of nerve fiber engagement by vagus nerve stimulation using physiological markers.* Brain Stimul, 2020. **13**(6): p. 1617-1630.

60. He, K., et al., *Mask R-CNN.* arXiv, 2017. **1703.06870**.
61. Zaqout, S., L.L. Becker, and A.M. Kaindl, *Immunofluorescence Staining of Paraffin Sections Step by Step.* Front Neuroanat, 2020. **14**: p. 582218.
62. Yuxin Wu, A.K., Francisco Massa, Wan-Yen Lo and and Ross Girshick. , *Detectron2.* 2019.
63. Viktor Tóth, N.J., Adam Abbas, Moontahinaz Rob, Ariba Khan, Stavros Zanos, Theodoros P. Zanos *Single-axon level segmentation and feature extraction pipeline combining traditional and deep learning computer vision algorithms.* Abstracts from the Fourth Bioelectronic Medicine Summit:, 2020: p. P16. .